Journal of Materials Chemistry A

ROYAL SOCIETY OF CHEMISTRY

PAPER

View Article Online
View Journal

Check for updates

Cite this: DOI: 10.1039/d6ta02361d

Vacancy-defective spinel $NiCo_2O_4$ enables high-valent Ni/Co species and adsorbate binding for the electrocatalytic upcycling of polybutylene succinate plastics

Jiahui Xian,[ab] Ziyu Mi,[ab] Panyawut Tonanon,[a] Xun Cao,[b] Richard D. Webster[a] and Wan Ru Leow*[ab]

Received 19th March 2026
Accepted 8th May 2026

DOI: 10.1039/d6ta02361d

rsc.li/materials-a

Electroreforming polybutylene succinate (PBS) plastic waste and NO_x into value-added chemicals is a promising strategy to mitigate environmental pollution. However, achieving high activity and controllable selectivity remains challenging especially at industrially relevant current densities, due to the complex multi-step dehydrogenation of alcohol intermediates and competing oxygen evolution reaction. Here, we report a vacancy-defective spinel-type $NiCo_2O_4$ electrocatalyst for the enhanced electrooxidation of 1,4-butanediol, a monomer derived from PBS plastic. Mechanistic studies revealed that the catalyst facilitates the generation of high-valent Ni/Co species and regulates the adsorption of oxygen-containing intermediates, thereby boosting catalytic activity *via* a OH*-participated mechanism. By pairing PBS hydrolysate oxidation with NO_x reduction reaction in a membrane electrode assembly, the system achieved a cell voltage of 1.42 V at 400 mA cm^{-2}, while maintaining continuous operation for over 100 hours with combined faradaic efficiencies exceeding 175%. High-purity SA and $NaHCO_3$ products can be separated from the post-reaction anolyte *via* CO_2-assisted acidification-precipitation. The obtained SA can further react with concentrated NH_3 in the catholyte to yield valuable succinimide. This work provides a practical approach for the efficient upcycling of sustainable plastic and NO_x into valuable products, enabled through tailored catalyst design and system configuration.

Wan Ru Leow

*Dr Leow Wan Ru is a Nanyang Assistant Professor in Nanyang Technological University and jointly a Principal Scientist in the Agency for Science, Technology and Research (A*STAR). She received her PhD in 2017 from the School of Materials Science and Engineering in Nanyang Technological University, after which she worked as a post-doctoral fellow in the Department of Electrical and Computer Engineering, University of Toronto. Her research interests are focused on the study and design of novel and efficient photocatalytic and electrocatalytic systems for decarbonized chemical conversions.*

Introduction

Plastics are ubiquitous in modern society due to low cost, widespread applications and durability.[1–3] However, the disposal of end-of-life plastics poses a significant problem – the environmental accumulation of plastic waste is projected to reach 12 000 million metric tons by 2050.[4–7] An example of such plastics is polybutylene succinate (PBS), with global production exceeding 120 000 tons per year due to applications in packaging, agriculture and textiles.[8,9] While it can be argued that PBS plastics are biodegradable, the degradation process is typically slow and converts a valuable carbon source into CO_2 emissions.[10,11] From a chemistry perspective, PBS is produced *via* the polycondensation of 1,4-butanediol (BDO) and succinic acid (SA), which means that end-of-life PBS represents a rich reservoir of valuable C_4 platform chemicals. SA is a vital C_4 diacids platform chemical for producing high-demand industrial commodities.[12,13] SA can also undergo amination to form succinimide, a privileged heterocyclic scaffold that is widely

[a]School of Chemistry, Chemical Engineering and Biotechnology, Nanyang Technological University, 21 Nanyang Link, Singapore 637371, Republic of Singapore. E-mail: wanru.leow@ntu.edu.sg

[b]Institute of Sustainability for Chemicals Energy and Environment (ISCE^2), Agency for Science, Technology and Research (A*STAR), 1 Pesek Road Jurong Island, Singapore 627833, Republic of Singapore

utilized as a versatile intermediate in organic synthesis and pharmaceutical development.[12] Thus, instead of conventional disposal or passive biodegradation, upcycling PBS into high-value chemicals offers a more sustainable strategy that simultaneously achieves plastic waste management and carbon resource recovery.

The electrocatalytic reforming of hydrolyzed polyester plastics into value-added chemicals, which can be powered by renewable electricity under mild conditions, has recently emerged as a sustainable and economically attractive route for plastic upcycling.[1,14–19] This typically involves the oxidation of binary primary alcohols to dicarboxylic acids, for which Ni-based materials have been extensively explored as efficient electrocatalysts, with *in situ* generated high-valent Ni species serving as the key active phase.[20–22] However, achieving high activity and controllable selectivity remains challenging especially at industrially relevant current densities, due to the complex multi-step dehydrogenation of alcohol intermediates and competing oxygen evolution reaction (OER).[23] Conversely, Co-based catalysts often exhibit oxidation activity at significantly lower onset potentials.[24] Thus, integrating Ni and Co sites is expected to generate a synergistic effect that can enhance activity and selectivity toward the oxidation of binary primary alcohols, while suppressing the competing OER through electronic redistribution and optimized adsorption strength.[25–27] To effectively harness such synergistic interactions, it is highly desirable to construct catalyst structures that can accommodate multiple catalytic sites, regulate their electronic structure and optimize alcohol oxidation while suppressing the competing OER. Spinel-type oxides have recently emerged as promising candidates in this regard, owing to their unique crystal framework that enables the coexistence of multiple metal cations in distinct coordination environments that facilitates efficient charge transfer and redox cycling.[28–30] These features make spinel oxides particularly attractive for polyol oxidation reactions involving complex multi-step dehydrogenation processes, in order to enable efficient and selective production of dicarboxylic acids.

In this work, we report a self-supported $NiCo_2O_4$ catalyst grown on nickel foam for enhanced electrocatalytic BDO oxidation reaction (BOR). The electrocatalyst achieved high faradaic efficiencies >87% towards SA across a wide current density range of 200–1000 mA cm^{-2}. *Operando* spectroelectrochemical studies and theoretical calculations reveal that the incorporation of Ni into the octahedral Co sites of spinel structures induces the formation of vacancy defects and electronic redistribution. This facilitates the *in situ* generation of CoOOH/NiOOH active species and optimizes the adsorption strength of oxygen-containing intermediates, thereby enhancing BOR catalytic activity *via* an *OH-mediated oxidation mechanism. We further demonstrated a paired electrocatalytic BOR||NO_xRR system for the simultaneous valorization of PBS hydrolysate and nitrogen oxide (NO_x) (Fig. 1a). Through a membrane electrode assembly (MEA), we achieved industrial-level current density of 400 mA cm^{-2} at a low voltage of 1.42 V, as well as 100 hours of stable operation with combined faradaic

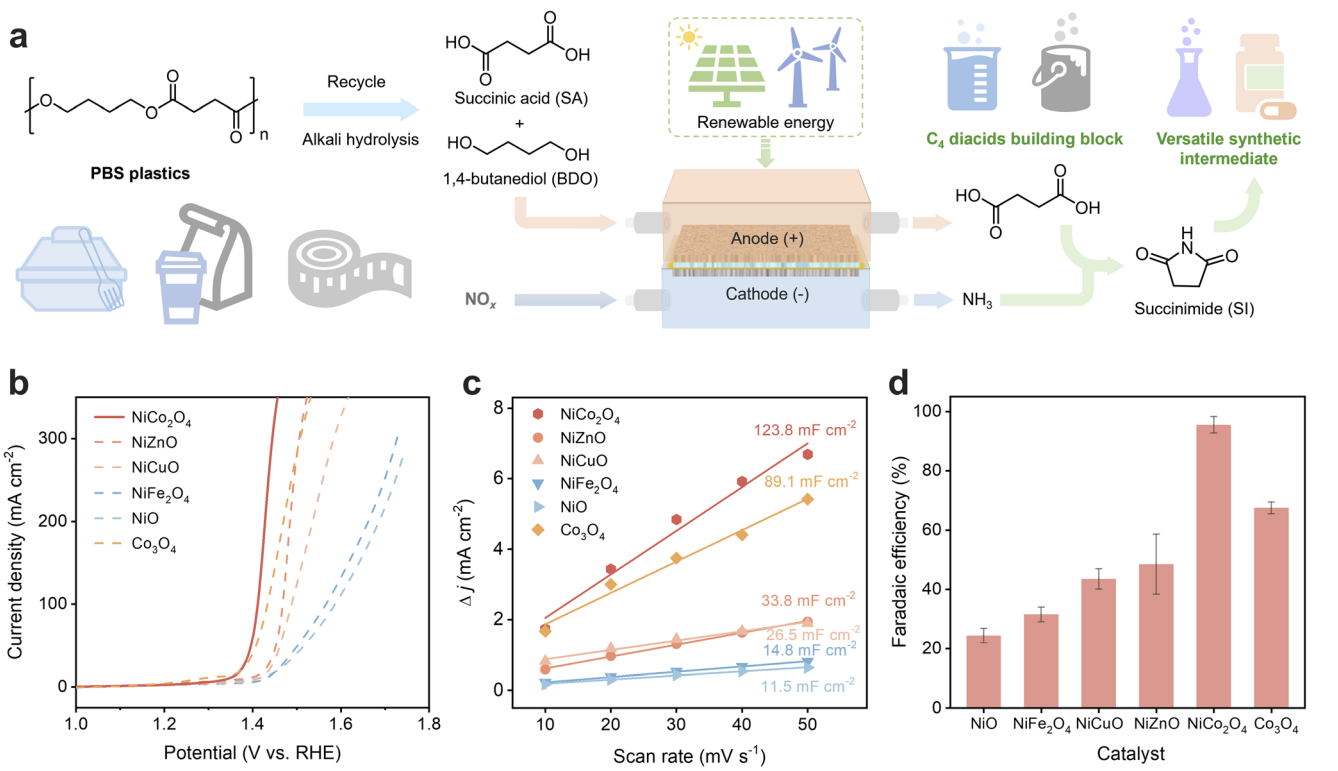

Fig. 1 (a) Schematic illustration of the paired BOR||NO_xRR system for electrocatalytic upgrading of waste pollutants. (b) LSV curves and (c) double layer capacitances of different catalysts for electrocatalytic BOR. (d) Faradaic efficiencies of SA over different electrocatalysts at 1.5 V *vs.* RHE.

efficiencies exceeding 175%. This is integrated with a CO_2-assisted precipitation that enables the recovery of high-purity SA and $NaHCO_3$ from the post-reaction anolyte. Techno-economic analysis (TEA) confirms the economic viability of this integrated electrocatalytic valorization and product separation system. The obtained SA can be further reacted with concentrated NH_3 in the catholyte to yield valuable succinimide.

Results

A series of M-doped nickel and cobalt oxides (M = Fe, Co, Cu, Zn) were synthesized on nickel foam (NF) substrate (defined as $Ni_xM_yO_z$) *via* a hydrothermal method followed by calcination, and their propensity for electrocatalytic BOR was screened in a three-electrode H-type cell. We first performed linear sweep voltammetry (LSV) to evaluate the electrocatalytic activity of catalysts. Compared to other synthesized electrocatalysts, $NiCo_2O_4$ exhibited a lower BOR potential of 1.41 V *vs.* RHE to reach the current density of 100 mA cm^{-2} (Fig. 1b). Additionally, $NiCo_2O_4$ showed the lowest Tafel slope of 54.6 mV dec^{-1} among all catalysts studied (Fig. S1), which suggests significantly faster BOR kinetics. The double-layer capacitance (C_{dl}) of $NiCo_2O_4$ is also significantly higher at 123.8 mF cm^{-2}, which indicates larger electrochemical active area and more exposed active sites (Fig. 1c and S2). The electrocatalytic BOR activity of the synthesized electrocatalysts was then evaluated through chronoamperometry at 1.50 V *vs.* RHE, in an electrolyte comprising 1.0 M NaOH and 0.1 M BDO, after which the liquid products were analyzed using ^1H nuclear magnetic resonance (NMR) spectroscopy (Fig. S3). Among all synthesized electrocatalysts, $NiCo_2O_4$ delivered SA as the main product with the highest activity, as reflected by its faradaic efficiency of 95.5(±2.8)%, selectivity of 89.2(±3.5)% and yield of 87.9(±4.5)% (Fig. 1d and S4). The electrocatalytic activity of Co_3O_4 and NiO are significantly inferior in comparison, which suggests a synergistic effect from integrating Ni and Co sites in $NiCo_2O_4$. Overall, the electrocatalytic activity of the synthesized electrocatalysts followed the trend: $NiCo_2O_4$ > Co_3O_4 > NiZnO > NiCuO > $NiFe_2O_4$ > NiO.

The electrocatalysts were then characterized to understand the difference in electrocatalytic activity. X-ray diffraction (XRD) revealed that the crystalline structures of the electrocatalysts were nickel-based or cobalt-based oxides (Fig. S5–S10). For $NiCo_2O_4$ and Co_3O_4, the diffraction peaks at 31.1°, 36.7°, 59.1° and 64.9° correspond to the (220), (311), (511) and (440) planes of the cubic spinel structure. Scanning electron microscopy (SEM) revealed the morphology of NiO, $NiFe_2O_4$, and NiZnO catalysts to be uniform nanosheets on the NF substrate (Fig. S5–S8). In contrast, the introduction of Co metal source during synthesis, such as in $NiCo_2O_4$ and Co_3O_4, led to a distinct one-dimensional nanostructure. Notably, the $NiCo_2O_4$ catalyst

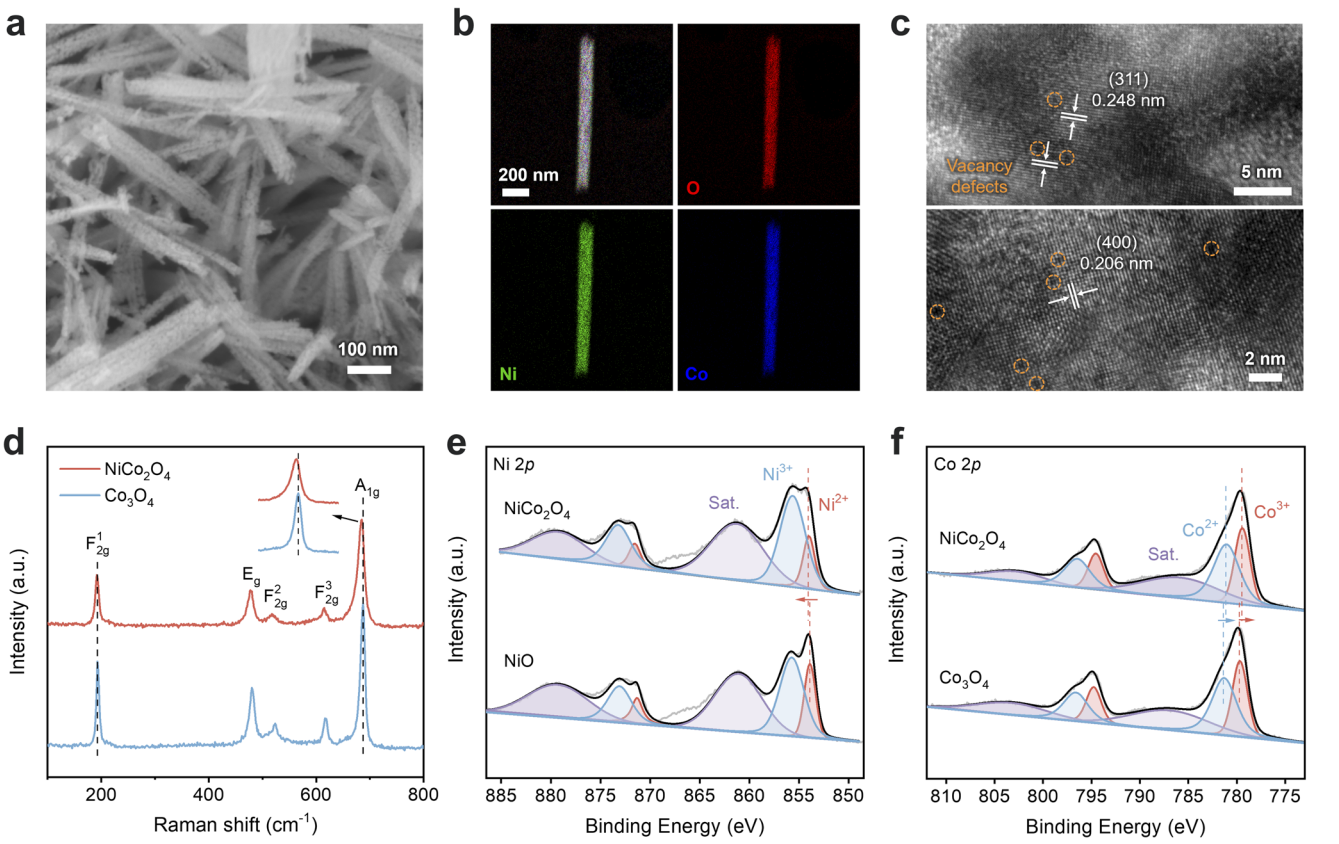

Fig. 2 (a) SEM, (b) TEM-EDS elemental mapping and (c) HRTEM images of $NiCo_2O_4$ electrocatalyst. (d) Raman spectra of $NiCo_2O_4$ and Co_3O_4. High-resolution XPS spectra of (e) Ni 2p and (f) Co 2p for $NiCo_2O_4$ and Co_3O_4.

existed as uniformly distributed nanowire arrays on the NF substrate (Fig. 2a and S11). Elemental mappings showed that Ni, Co and O were uniformly distributed throughout the whole nanowire (Fig. 2b). High-resolution transmission electron microscopy (HRTEM) images display distinct lattice spacings of 0.248 nm and 0.206 nm, which can be assigned to the (311) and (400) planes of $NiCo_2O_4$ (Fig. 2c). Abundant vacancy defects were observed by HRTEM and corresponding integrated pixel intensity profile (Fig. 2c and S12). These defects likely originated from the partial substitution of Co with Ni of similar cation radius, which would provide abundant active sites for the adsorption and activation of oxygen-containing intermediates.[29]

The Raman spectra of $NiCo_2O_4$ and Co_3O_4 exhibit five typical characteristic peaks in 191.4, 477.8, 517.3, 615.1 and 684.8 cm^{-1}, corresponding to the $F_{2g}{}^1$, E_g, $F_{2g}{}^2$, $F_{2g}{}^3$ and A_{1g} vibrational modes of spinel Co_3O_4, respectively (Fig. 2d). The $F_{2g}{}^1$ and A_{1g} signals can be attributed to the asymmetric and symmetrical stretching vibration of Co^{2+}–O bond in tetrahedral coordination sites and Co^{3+}–O bond in octahedral coordination sites, respectively. Compared to Co_3O_4, the $NiCo_2O_4$ showed an obvious redshift in its A_{1g} Raman signal, while its $F_{2g}{}^1$ signal remained unshifted, which suggests that the incorporated Ni mainly occupied the octahedral coordination sites. Meanwhile, the broader and weaker A_{1g} signal in $NiCo_2O_4$ indicates lattice distortion or deficient coordination due to Ni incorporation into the Co_3O_4 lattice, which promotes the formation of vacancy defects.[29,31] The high-resolution Ni 2p X-ray photoelectron spectroscopy (XPS) spectra can be deconvoluted into two spin–orbit doublets corresponding to Ni^{2+} (854.0 and 871.5 eV) and Ni^{3+} (855.6 and 873.2 eV), along with the accompanying satellite peaks (Fig. 2e and Table S1). Notably, the Ni^{2+} 2p peaks in $NiCo_2O_4$ shifted to higher binding energy compared to that in NiO, which suggests electronic interaction between Ni and the Co. On the other hand, Co 2p XPS spectra displayed two characteristic spin-orbital doublets at approximately 779.4/794.6 eV and 781.1/796.5 eV, which can be attributed to Co^{3+} and Co^{2+} respectively. A negative shift of ~0.3 eV was observed for the Co 2p peaks in $NiCo_2O_4$ relative to those in Co_3O_4, and the ratio of Co^{2+}/Co^{3+} in $NiCo_2O_4$ (1.48) is higher than that of Co_3O_4 (1.41), which suggests the formation of lower Co valence state (Fig. 2f and Table S2). These results further indicate that the introduced Ni atoms preferentially occupy the octahedral Co^{3+} sites within the spinel lattice, which is in agreement with the observed Raman shifts. The O 1s spectra of the electrocatalysts show three peaks at 529.4, 531.0 and 532.7 eV (Fig. S13 and Table S3), corresponding to the lattice oxygen (O_a), chemisorbed oxygen (O_b) and surface oxygen (O_c), respectively. $NiCo_2O_4$ exhibits higher O_b/O_a ratio, suggesting increased surface oxygen vacancies when the spinel lattice was disrupted through the introduction of Ni atoms.[32] The electron paramagnetic resonance (EPR) spectrum of $NiCo_2O_4$ exhibits a distinct and symmetric Lorentzian-shaped signal, a feature characteristic of electrons trapped in oxygen vacancies, while a much weaker signal was observed for Co_3O_4 (Fig. S14). The above results confirm that

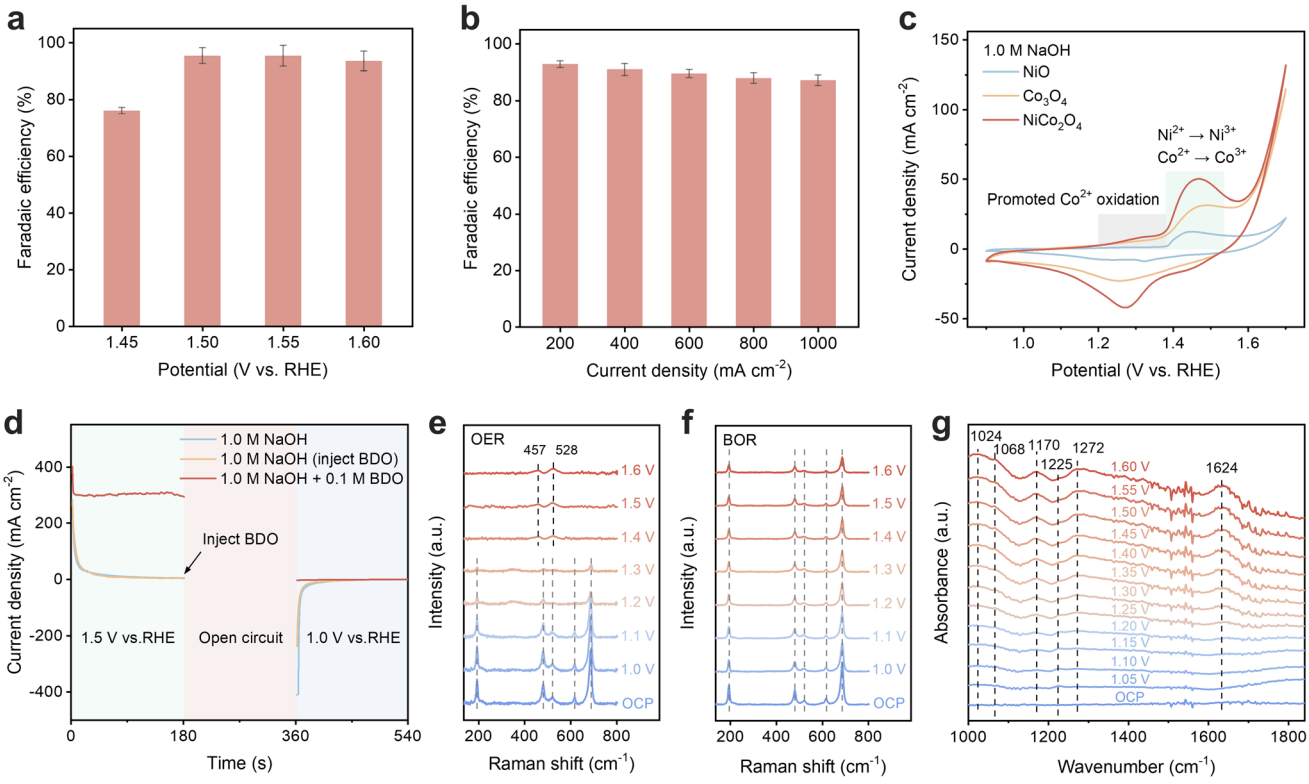

Fig. 3 Faradaic efficiencies of SA over $NiCo_2O_4$ at different (a) potentials and (b) current densities. (c) CV curves of $NiCo_2O_4$, Co_3O_4 and NiO in 1 M NaOH solution. (d) Multipotential-step curves of $NiCo_2O_4$ in 1.0 M NaOH solution with and without 0.1 M BDO injection. *In situ* Raman spectra of $NiCo_2O_4$ for (e) OER and (f) BOR at varied potentials. (g) *In situ* FTIR spectra of $NiCo_2O_4$ during the BOR at various potentials.

introducing Ni into the Co_3O_4 spinel structure endows $NiCo_2O_4$ with abundant electroactive sites and vacancy defects, which is crucial for boosting the electrocatalytic BOR performance.

Having established the nature of the $NiCo_2O_4$ electrocatalyst, we investigated its electrochemical BOR activity in 1.0 M NaOH containing 0.1 M BDO electrolyte. Upon increasing the applied potential from 1.45 V to 1.50 V *vs.* RHE, the faradaic efficiency towards SA significantly increased from 76.1(±1.1)% to 95.5(±2.8)%, and the yield rose from 51.6 (±2.5)% to 87.9 (±4.5)%. Beyond 1.50 V *vs.* RHE, $NiCo_2O_4$ exhibited superior SA production with up to 96.0% faradaic efficiency, 95.4% yield and 95.6% selectivity (Fig. 3a and S15), which is competitive with that of previously reported catalysts (Table S4). This means that SA productivity can remain high across a wide range of current densities (200–1000 mA cm^{-2}), with faradaic efficiencies >87%, yields >90% and selectivities >93% (Fig. 3b and S16).

Cyclic voltammetry (CV) revealed a characteristic anodic peak located from 1.35 to 1.45 V *vs.* RHE, which can be attributed to the oxidation of Ni^{2+}/Ni^{3+} and Co^{2+}/Co^{3+} redox couples.[33] The incorporation of Ni promotes the pre-oxidation of Co^{2+}, thereby enhancing the BOR activity, as evidenced by the appearance of a distinct Co^{2+} pre-oxidation peak at ~1.28 V *vs.* RHE and more intense oxidation peak in $NiCo_2O_4$ compared to Co_3O_4 (Fig. 3c). Upon the addition of 0.1 M BDO, these oxidation peaks disappear and the anodic current density increases sharply, which confirms the involvement of active Ni and Co species in electrocatalytic BOR (Fig. S17). The CV curves can also provide insights on the adsorption behavior of *OH on the $NiCo_2O_4$ electrocatalyst.[20,34] Regardless of BDO addition, $NiCo_2O_4$ electrocatalyst exhibited a higher peak oxidation current for $OH^- \rightarrow$ *OH compared to Co_3O_4 (Fig. S18), indicating that Ni incorporation enhances the generation and adsorption of *OH species. We performed quasi-*in situ* EPR using DMPO (5,5-dimethyl-1-pyrroline *N*-oxide) as a spin-trapping agent, and observed the characteristic 1 : 2 : 2 : 1 quartet signal for DMPO-*OH adduct in the absence of BDO at 1.5 V *vs.* RHE for 5 min. This provides direct evidence for the electrochemical conversion of OH^- to *OH. Upon the addition of BDO, the DMPO-*OH signal intensity decreased and DMPO-*R signal appeared, indicating the involvement of *OH in the electrocatalytic BOR process (Fig. S19).

Operando electrochemical impedance spectroscopy (EIS) was conducted to further investigate high electrocatalytic BOR activity (Fig. S20). The Bode plots exhibited distinct features in the high-frequency region under potentials of 1.05–1.40 V *vs.* RHE, corresponding to the electrooxidation of Ni^{2+}/Co^{2+} to Ni^{3+}/Co^{3+}. In the presence of BDO, low-frequency signals emerged at potentials above 1.35 V *vs.* RHE, which suggests that the BOR becomes the dominant electrochemical process. With increasing applied potentials, the lower phase angles indicate more favorable BOR than OER, as well as enhanced interface reactivity. This implies rapid oxidation of absorbed BDO molecules with faster interfacial charge transfer without OER interference. We also observed lower phase angles for $NiCo_2O_4$ compared to Co_3O_4, which meant that introducing Ni into the Co_3O_4 cubic spinel structure led to increased BOR activity.

We further probed this electrooxidation mechanism by performing a multipotential-step experiment on the $NiCo_2O_4$ catalyst. The protocol is as follows: (i) 1.5 V *vs.* RHE to generate high-valent Ni/Co oxidized species, (ii) open circuit potential (OCP), and finally (iii) 1.0 V *vs.* RHE (Fig. 3d). In the control experiment without BDO, the high-valent Ni/Co oxidized species would revert back to their original valence state at 1.0 V *vs.* RHE, leading to the observation of a reduction current. With BDO injection at OCP, this reduction current at 1.0 V *vs.* RHE was smaller, which means that BDO reacted with the electrogenerated high-valent Ni/Co species and caused them to be rapidly consumed. No significant reduction current can be detected if BDO is present from the start, which means that BDO can immediately consume the electrogenerated active species once formed. We then employed *in situ* Raman spectroscopy to gain further insight into the dynamic structural evolution and active sites. For the OER process, $NiCo_2O_4$ displays five characteristic peaks at OCP, which are associated with the vibrational modes of $NiCo_2O_4$ spinel structure. As the potential increased to 1.3 V *vs.* RHE, these peaks gradually diminished. Two new peaks at approximately 457 and 528 cm^{-1} emerged at 1.4 V *vs.* RHE and slightly intensified with increased potential, which correspond to the E_g and A_{1g} vibrational modes of Co^{3+}–O/Ni^{3+}–O bond in CoOOH/NiOOH species (Fig. 3e).[26,34] These potential-dependent Raman shifts confirm the *in situ* structural reconstruction of $NiCo_2O_4$ under OER condition, leading to the formation of high-valent Ni/Co (oxy)hydroxide species (CoOOH/NiOOH). In contrast, the $NiCo_2O_4$ catalyst retained its original spinel structure during BOR. No characteristic peaks for Co^{3+}–O/Ni^{3+}–O bonds were detected, and the signature peaks of $NiCo_2O_4$ remained across the entire potential range from OCP to 1.6 V *vs.* RHE (Fig. 3f). This indicates that BDO molecules react instantly with CoOOH/NiOOH species once generated, such that the consumption rate of these species exceeds the generation rate, which suppresses the competing OER and enables continuously electrogenerated highly active species for efficient BOR. Combining the insights from cyclic voltammetry, multipotential-step experiment and Raman spectroscopy, this suggests that enhanced generation and adsorption of *OH species is favorable for the BOR mechanism, which can be achieved through the abundant electroactive sites and vacancy defects in $NiCo_2O_4$.

We further tracked the potential-dependent evolution of adsorbed intermediates and products over $NiCo_2O_4$ catalyst using *in situ* attenuated total reflection surface-enhanced infrared absorption spectroscopy (ATR-SEIRAS). The peak at 1024 cm^{-1} can be attributed to the C–OH stretching vibration of BDO.[22,23] The increase in intensity as the potential shifts from OCP to 1.6 V *vs.* RHE can be attributed to increased adsorption of BDO on catalyst surface. The peaks at 1225 cm^{-1} and 1170 cm^{-1} can be assigned to the C–O stretching vibration of the generated oxygenated molecules. The 1225 cm^{-1} peak appeared at 1.05 V *vs.* RHE, while the 1170 cm^{-1} peak emerged at 1.10 V *vs.* RHE and continuously increased up to 1.60 V *vs.* RHE. This coincides with the onset potential for the formation of *OH, which further confirms the role of *OH in generating oxygenated molecules during the electrocatalytic BOR process.

The peak at 1068 cm^{-1}, which can be attributed to the stretching vibration of the aldehyde group, increased in intensity from 1.25 V *vs.* RHE, which implies that BDO was first oxidized to 4-hydroxybutyric acid.[35,36] Two distinct peaks at 1272 and 1624 cm^{-1}, which can be assigned to the C–O and C═O stretching vibration of carboxylate, were also observed at 1.25 V *vs.* RHE and increased with increasing potential, indicating the generation of SA product (Fig. 3g).[35–37]

We corroborated our experimental results with density functional theory (DFT) calculations performed on the optimized stable $NiCo_2O_4$ and Co_3O_4 model slabs (Fig. S21). As the effective regulation of adsorption behavior is critical for achieving highly selective oxidation, the adsorption of BDO and *OH on the octahedral sites were investigated. For *OH, the octahedral Co sites on $NiCo_2O_4$ exhibit markedly stronger adsorption (−1.59 eV) than the Co sites on Co_3O_4 (−0.79 eV) and the Ni sites on $NiCo_2O_4$ (−0.98 eV) (Fig. 4a and S22). A similar phenomenon is observed for BDO adsorption, with the octahedral Co sites on $NiCo_2O_4$ showing the strongest binding (Fig. 4b and S23). Projected density of states (PDOS) analysis reveals significant orbital hybridization between Co/Ni 3d and O 2p states in $NiCo_2O_4$, suggesting an altered electronic configuration of the adjacent Co atoms upon Ni incorporation. The d-band center (ε_d) of the $NiCo_2O_4$ (−1.43 eV) is closer to the Fermi level than the Co_3O_4 (−1.82 eV), indicating stronger antibonding interactions and consequently enhanced adsorption of BDO and *OH species (Fig. 4c). These results collectively demonstrate that Ni incorporation at the octahedral Co sites regulates the electronic structure and enhances the adsorption of oxygen-containing intermediates, thereby promoting the catalytic BOR process. Based on the above evidence, we propose an *OH-participated oxidation pathway (Fig. 4d). Under the electrochemical driving force, BDO molecules and hydroxyl species are initially adsorbed onto the catalyst surface, such that OH^- from the electrolyte is converted into surface-bound *OH at the active sites. The generated *OH subsequently attacks the alcoholic hydroxyl groups of the adsorbed BDO molecules,

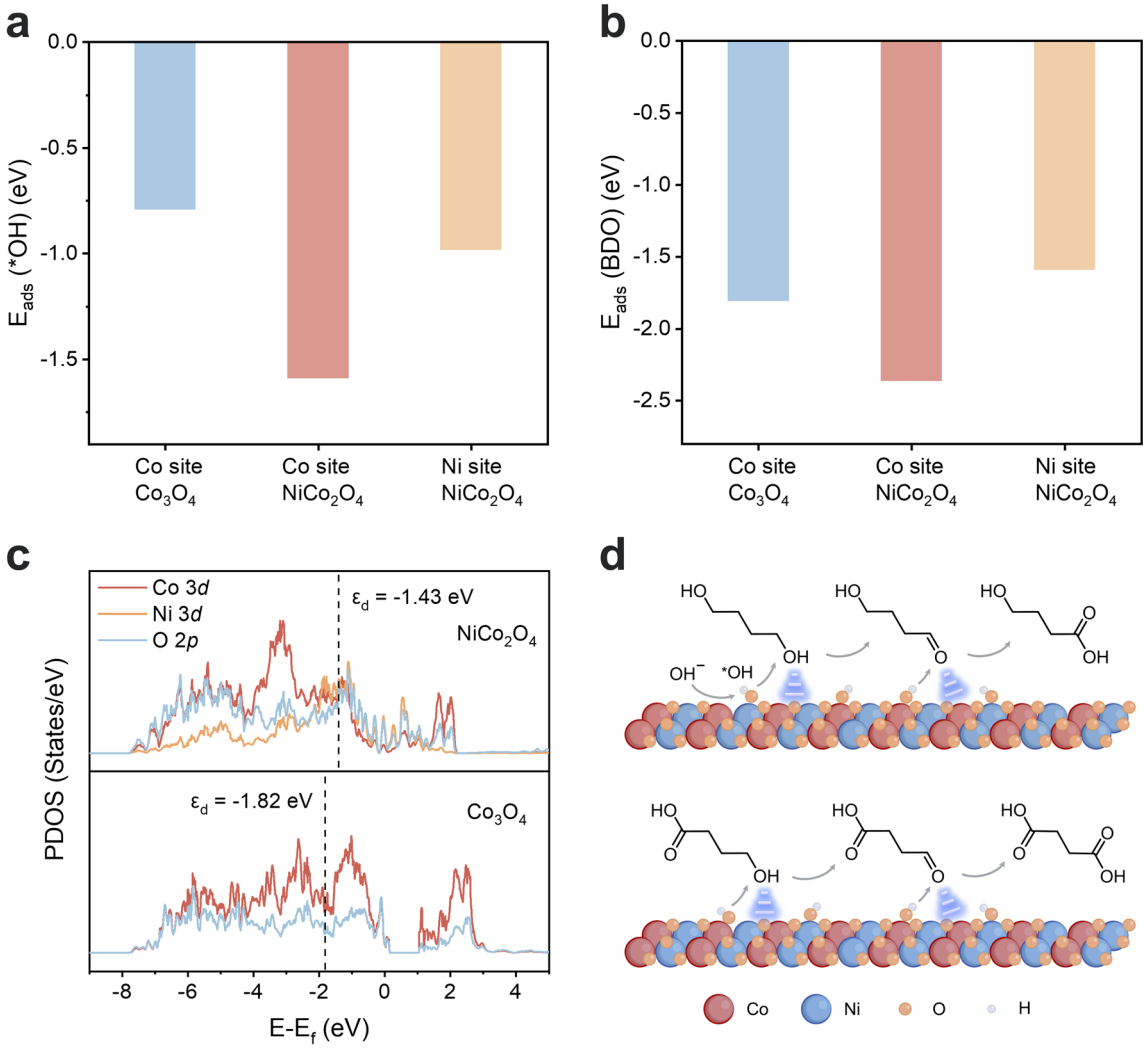

Fig. 4 The calculated adsorption energies of (a) *OH and (b) BDO on $NiCo_2O_4$ and Co_3O_4. (c) PDOS profiles of $NiCo_2O_4$ and Co_3O_4. (d) Schematic illustration of the proposed BOR pathways on the $NiCo_2O_4$ electrocatalyst.

followed by continual oxidative deprotonation to ultimately generate SA product.

Finally, we realized overall waste PBS recycling by integrating electrochemical BOR and PBS hydrolysis. The obtained PBS hydrolysate contained only BDO and SA monomers (Fig. S24), which directly served as the anolyte without further purification. The subsequent electrocatalytic upgrading of PBS hydrolysate was coupled with cathodic NO_x reduction, to enable simultaneous valorization of two waste streams into valuable chemicals with improved energy efficiency and process economics at the industrial scale.[38,39] This paired BOR||NO_2^-RR system was assembled using a membrane electrode assembly (MEA) electrolyzer, comprising a $NiCo_2O_4$ anode and an oxide-derived Cu cathode coated on copper foam (OD-Cu) (Fig. S25). The OD-Cu cathode was fabricated by electrochemically reducing the pre-deposited Cu_xO array (see characterization in Fig. S26). The assembled BOR||NO_2^-RR electrolyzer achieved an industrial current density of 400 mA cm^{-2} at a low cell voltage of 1.42 V (Fig. 5a). This cell voltage is significantly lower than that of the BOR||HER electrolyzer, which signifies improved reaction kinetics and energy efficiency. The paired-electrosynthesis system demonstrated robust durability, maintaining faradaic efficiencies averaging 87.3% and 90.7% towards SA and NH_3 for over 100 hours at an industrial current density of 400 mA cm^{-2} (Fig. 5b). ^{1}H NMR analysis confirms that BDO is predominantly converted to SA (Fig. S27). Ultimately, 27.4 g SA was obtained from 30 g of PBS plastic, with the simultaneous generation of 0.125 M NH_3 in the catholyte. Post-reaction characterization of the $NiCo_2O_4$ anode and OD-Cu/CF cathode showed little change in structure and morphology (Fig. S28 and S29).

We then employed a CO_2-assisted sequential precipitation method to separate SA from the alkaline electrolyte, which simultaneously yielded $NaHCO_3$ as a product (Fig. S30).[22,40] Specifically, excess CO_2 is introduced into the resulting anolyte until the pH reaches 7.8. This neutralized OH^- and led to the precipitation of low-solubility $NaHCO_3$, thereby effectively removing Na^+ ions from solution. Hydrochloric acid is added to convert sodium succinate into SA, which can be precipitated by cooling to 2–8 °C due to its lower solubility. Overall, this process enabled the recovery of 0.92 g SA (Fig. 5c and S31) and 5.1 g $NaHCO_3$ (Fig. S32) from 100 mL of crude anolyte. Techno-economic analysis (TEA) showed that this technology can be economically viable if we assume an electricity cost of \$0.1 kWh^{-1} and faradaic efficiency exceeding 35% (Fig. S33). Our calculations estimate a net revenue of \$602.2 per ton of SA based on electrochemical performance close to that achieved in the MEA (*i.e.*, faradaic efficiencies of 90% towards SA and NH_3 at current density 400 mA cm^{-2}, cell voltage 1.5 V) (Fig. 5d). The high-purity SA obtained is itself an important platform chemical, but can also react with concentrated NH_3 in the catholyte to generated succinimide (Fig. 5e and S34), which is a versatile organic synthetic intermediate.

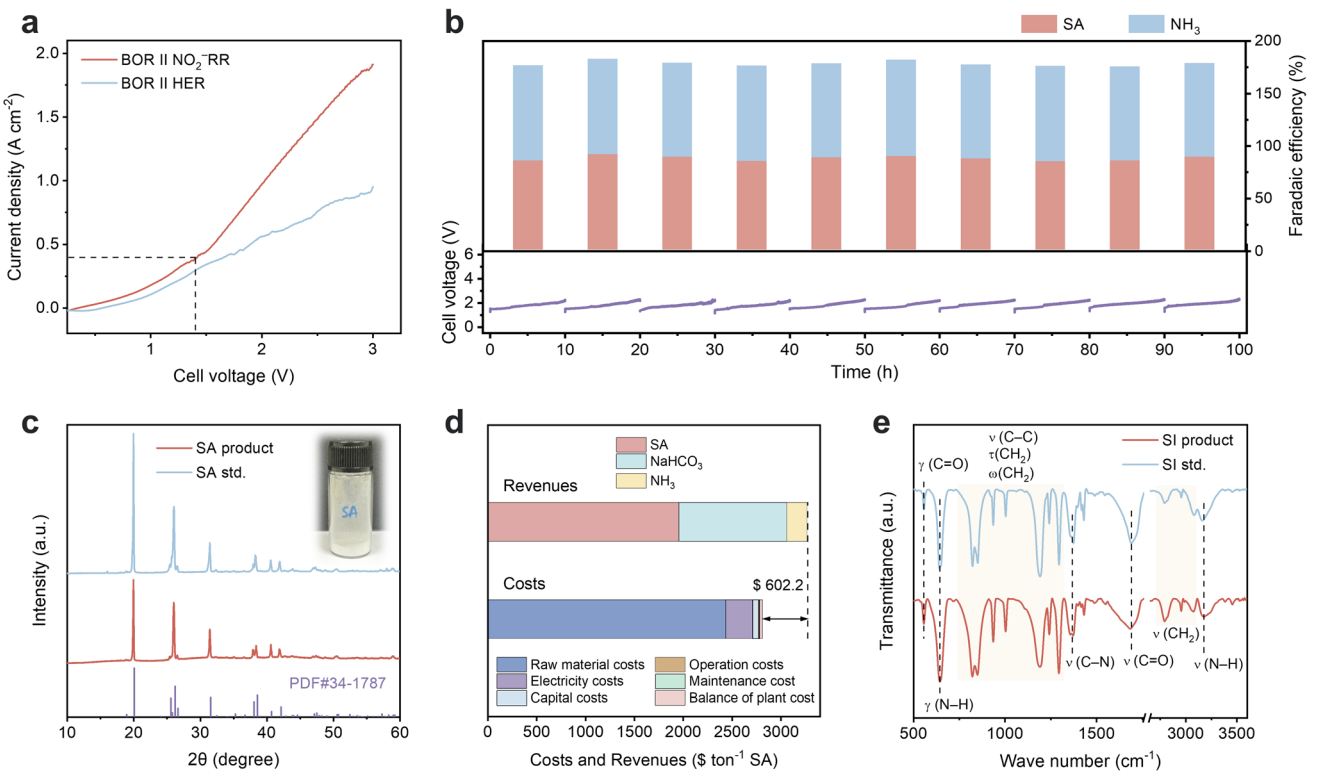

Fig. 5 (a) LSV curves of the paired BOR||NO_2^-RR and BOR||HER systems. (b) Electrochemical upgrading of PBS hydrolysate and NO_x in the MEA electrolyzer at 400 mA cm^{-2} for 100 hours. (c) XRD patterns of obtained SA product and standard (inset: photograph of the product). (d) TEA of BOR||NO_2^-RR electro-upgrading system from PBS plastics. (e) FT-IR spectra of obtained SI product and standard.

Discussion

In summary, we report a self-supported $NiCo_2O_4$ electrocatalyst featuring vacancy defect sites and electronic structure rearrangement, for the electrocatalytic valorization of PBS-derived BDO. The catalyst achieved an industrial-level current density of 1 A cm^{-2}, along with a high faradaic efficiency (>87%) and yield (>90%) of SA. Both experimental and DFT studies revealed that incorporating Ni into Co octahedral sites modulated the electronic structure and d-band center, which strengthened the adsorption of oxygen-containing intermediates and facilitated pre-oxidation into CoOOH/NiOOH active species, thereby boosting BOR activity *via* an *OH-participated oxidation mechanism. We assembled a paired BOR||NO_2^-RR system in an MEA configuration, which required only 1.42 V to reach an industrial-level current density of 400 mA cm^{-2}. The stability of the paired BOR||NO_2^-RR system was demonstrated through continuous electro-upgrading of PBS-plastic hydrolysate and NO_x waste at faradaic efficiencies averaging 87.3% and 90.7% for over 100 hours. High-purity SA and $NaHCO_3$ products can be efficiently obtained from the post-reaction anolyte *via* the CO_2-assisted sequential precipitation method. The obtained SA can be further converted to succinimide through reaction with concentrated NH_3 in the catholyte. This work presents a practical approach for the electrocatalytic conversion of PBS plastic and NO_x waste into valuable products through tailored catalyst design and system configuration.

Author contributions

W. R. L. and J. X. conceived the idea, designed the experiments, and co-wrote the manuscript. W. R. L. supervised the project. J. X. carried out the material synthesis and characterization, electrochemical measurements, and analyzed the data. Z. M. performed SEM measurement. P. T. and R. D. W. performed the EPR measurement. X. C. performed TEM characterization. All authors discussed the results and assisted during manuscript preparation.

Conflicts of interest

The authors declare no competing interests.

Data availability

The data supporting this article have been included as part of the supplementary information (SI). Supplementary information: experimental methods, additional characterization data, additional electrochemical results, and supplementary figures and tables. See DOI: https://doi.org/10.1039/d6ta02361d.

Acknowledgements

This work is supported by the National Research Foundation Fellowship (NRFF16-2024-0034).

References

1 K. Zheng, Y. Wu, Z. Hu, S. Wang, X. Jiao, J. Zhu, Y. Sun and Y. Xie, *Chem. Soc. Rev.*, 2023, **52**, 8–29.
2 On the plastics crisis, *Nat. Sustain.*, 2023, **6**, 1137.
3 J. Chen, L. Zhang, L. Wang, M. Kuang, S. Wang and J. Yang, *Matter*, 2023, **6**, 3322–3347.
4 R. Geyer, J. R. Jambeck and K. L. Law, *Sci. Adv.*, 2017, **3**, e1700782.
5 L. D. Ellis, N. A. Rorrer, K. P. Sullivan, M. Otto, J. E. McGeehan, Y. Román-Leshkov, N. Wierckx and G. T. Beckham, *Nat. Catal.*, 2021, **4**, 539–556.
6 M.-Q. Zhang, M. Wang, B. Sun, C. Hu, D. Xiao and D. Ma, *Chem*, 2022, **8**, 2912–2923.
7 D. M. Mitrano and M. Wagner, *Nat. Rev. Mater.*, 2021, **7**, 71–73.
8 D. Nath, M. Misra, F. Al-Daoud and A. K. Mohanty, *RSC Sustain.*, 2025, **3**, 1267–1302.
9 Industry Research, https://www.industryresearch.biz/market-reports/polybutylene-succinate-market-114054, accessed March 2026.
10 T.-Y. Liu, D. Huang, P.-Y. Xu, B. Lu, G.-X. Wang, Z.-C. Zhen and J. Ji, *ACS Sustainable Chem. Eng.*, 2022, **10**, 3191–3202.
11 Y. Zhu, X. Che, F. Yuan, R. Jia, P. Chen, L. Shi and L. Huang, *Ind. Eng. Chem. Res.*, 2025, **64**, 4627–4636.
12 V. Kumar, P. Kumar, S. K. Maity, D. Agrawal, V. Narisetty, S. Jacob, G. Kumar, S. K. Bhatia, D. Kumar and V. Vivekanand, *Biotechnol. Biofuels*, 2024, **17**, 72.
13 W. Dessie, X. Luo, G. J. Duns, M. Wang and Z. Qin, *Environ. Technol. Innov.*, 2023, **32**, 103243.
14 Q. Hu, Z. Zhang, D. He, J. Wu, J. Ding, Q. Chen, X. Jiao and Y. Xie, *J. Am. Chem. Soc.*, 2024, **146**, 16950–16962.
15 S. Zhang, M. Li, Z. Zuo and Z. Niu, *Green Chem.*, 2023, **25**, 6949–6970.
16 D. Sajwan, A. Sharma, M. Sharma and V. Krishnan, *ACS Catal.*, 2024, **14**, 4865–4926.
17 Y. X. Leiu, K. M. Lim, Z. J. Chiah, E. S. Z. Mah and W. J. Ong, *EcoEnergy*, 2024, **3**, 217–253.
18 S. Yue, P. Wang, B. Yu, T. Zhang, Z. Zhao, Y. Li and S. Zhan, *Adv. Energy Mater.*, 2023, **13**, 2302008.
19 H. Wu, H. Tian, L. Chen, W. Luo, S. Li, L. Wang, X. Cui and J. Shi, *Adv. Mater.*, 2026, **38**, e15766.
20 Q. Qian, X. He, Z. Li, Y. Chen, Y. Feng, M. Cheng, H. Zhang, W. Wang, C. Xiao, G. Zhang and Y. Xie, *Adv. Mater.*, 2023, **35**, e2300935.
21 M. Song, Y. Wu, Z. Zhao, M. Zheng, C. Wang and J. Lu, *Adv. Mater.*, 2024, **36**, e2403234.
22 B. Zhou, K. Shi, X. Teng, Z. Li, L. Chen and J. Shi, *Angew. Chem., Int. Ed.*, 2024, **63**, e202411502.
23 J. Yan, Y. Ren, B. Huang, Z. Li, C. Zhao, L. Chen and J. Shi, *J. Am. Chem. Soc.*, 2025, **147**, 29340–29348.
24 Y. Lu, T. Liu, C. L. Dong, C. Yang, L. Zhou, Y. C. Huang, Y. Li, B. Zhou, Y. Zou and S. Wang, *Adv. Mater.*, 2022, **34**, e2107185.
25 D. Chen, Y. Ding, X. Cao and L. Sun, *Appl. Catal., B*, 2025, **378**, 125539.

26 J. Woo, J. Choi, J. Choi, M. Y. Lee, E. Kim, S. Yun, S. Yoo, E. Lee, U. Lee, D. H. Won, J. H. Park, Y. J. Hwang, J. S. Yoo and D. K. Lee, *Adv. Funct. Mater.*, 2025, **35**, 2413951.
27 W. Wang, X. He, Z. Tu, D. Xiong, S. Dong, T. Zhang, D. Wu, J. Wang and Z. Chen, *ACS Catal.*, 2025, **15**, 9574–9583.
28 B. He, F. Bai, P. Jain and T. Li, *Small*, 2025, **21**, e2411479.
29 W. Luo, H. Tian, Q. Li, G. Meng, Z. Chang, C. Chen, R. Shen, X. Yu, L. Zhu, F. Kong, X. Cui and J. Shi, *Adv. Funct. Mater.*, 2024, **34**, 2306995.
30 M. Wang, X. Feng, S. Li, Y. Ma, Y. Peng, S. Yang, Y. Liu, H. Lei, J. Dang, W. Zhang, R. Cao and H. Zheng, *Adv. Funct. Mater.*, 2024, **34**, 2410439.
31 Z. Chen, G. Zhang, H. Yang, Y. Zhao, A. Pei, P. Wang, J. Yang, J. Zhang, P. Sun, H. Qin, J. Zhan, J. Peng, W. H. Huang, L. Zhou and G. Chen, *ACS Nano*, 2025, **19**, 26572–26582.
32 R. An, C. Wang, Y. Li, Y. Di, F. Li, F. Li, L. Sun and X. Wu, *ACS Nano*, 2025, **19**, 17490–17502.
33 M. Jiang, Y. Yang, Y. Wang, Y. Wang, M. Ratova and D. Wu, *Green Chem.*, 2025, **27**, 9978–9991.
34 X. Jiang, X. Ma, Y. Yang, Y. Liu, Y. Liu, L. Zhao, P. Wang, Y. Zhang, Y. Lin and Y. Wei, *Nano-Micro Lett.*, 2024, **16**, 275.
35 F. Kang, Q. Wang, D. Du, L. Wu, D. W. F. Cheung and J. Luo, *Angew. Chem., Int. Ed.*, 2025, **64**, e202417648.
36 D. Du, P. Liu, Z. Teng, T. Chen, J. Zhu, B. Shao and J. Luo, *ACS Catal.*, 2025, **15**, 3038–3045.
37 X. Jiang, K. Zhao, H. Feng, L. Ke, X. Wang, Y. Liu, L. Li, P. Sun, Z. Chen, Y. Sun, Z. Wang, L. Yu and N. Yan, *J. Am. Chem. Soc.*, 2025, **147**, 13471–13482.
38 L. Xia, K. Zhao, S. Kadam, M. D. Blanco-González, M. D. Hernández Alonso and F. P. García de Arquer, *Joule*, 2025, **9**, 102049.
39 J. Qi, Y. Xia, X. Meng, J. Li, S. Yang, H. Zou, Y. Ma, Y. Zhang, Y. Du, L. Zhang, Z. Lin and J. Qiu, *Adv. Mater.*, 2025, **37**, e2419058.
40 D. Xiong, X. He, Z. Zhu, T. Liu, D. Wu, Y. Zou and Z. Chen, *Adv. Funct. Mater.*, 2026, **36**, e18434.